Journal of Sound and Vibration 608 (2025) 119061

Contents lists available at ScienceDirect

Journal of Sound and Vibration

journal homepage: www.elsevier.com/locate/jsvi

Zero-stiffness in rolling-lobe air springs for passive, load adaptable and low-frequency vibration isolation

Moritz Sprengholz *, Christian Hühne

Technische Universität Braunschweig, Institute of Mechanics and Adaptronics, Langer Kamp 6, 38106, Braunschweig, Germany

ARTICLE INFO

Dataset link: https://zenodo.org/doi/10.5281/zenodo.13777799

Keywords:
Zero-stiffness
Load adaptability
Passive vibration isolation
Rolling-lobe air spring isolator
3D-printing

ABSTRACT

Low-frequency vibration isolation is crucial for engineering structures and devices susceptible to low-frequency vibrations. Traditional linear isolators fail to provide effective low-frequency isolation without compromising static load capacity. At the same time, quasi-zero-stiffness designs struggle with load adaptability, maintaining zero-stiffness over a large displacement range, or require active components to achieve the former. Combining all of these features, this study investigates rolling-lobe air spring isolators as a passive vibration isolation alternative, aiming to achieve zero-stiffness across a wide displacement range under varying loads. To identify factors affecting vibration isolation performance in rolling-lobe isolators, this research examines various design parameters, including isolator geometry, internal pressure, external volume and membrane behavior. These parameters' influence on the stiffness and damping characteristics is investigated through a rapid prototyping approach employing 3D-printing to fabricate and test 86 unique isolator configurations. The experimental data informs a predictive model based on a Duffing oscillator, which is then applied in single degree-of-freedom simulations to assess isolation efficiency across different loads and excitation levels. The simulation results demonstrate effective isolation from close to 2 Hz onwards for the most promising configuration. Key findings are that higher internal pressures, controlled membrane deformation, and the addition of external volumes greatly enhance isolation performance. These insights provide valuable guidelines for designing rolling-lobe isolators capable of achieving zero-stiffness under varying loads and excitation levels, making them suitable for applications demanding robust passive vibration isolation over a broad range of operating conditions.

1. Introduction to advanced vibration isolation techniques

Linear vibration isolators begin to effectively isolate at frequencies exceeding $\sqrt{2}$ times their natural frequency, which is primarily determined by the isolator's stiffness [1]. Achieving a low natural frequency significantly enhances isolation quality [2] but requires extremely low stiffness, leading to large static deformations under the system's own weight [1,3]. This trade-off limits the effectiveness of linear isolators in applications requiring both high static load support and low dynamic stiffness, as encountered in aerospace, automotive and robotic systems [2,4].

* Corresponding author.
E-mail address: m.sprengholz@tu-braunschweig.de (M. Sprengholz).

https://doi.org/10.1016/j.jsv.2025.119061
Received 20 November 2024; Received in revised form 31 January 2025; Accepted 7 March 2025
Available online 16 March 2025

1.1. Quasi-zero-stiffness isolators

Addressing the limitations of linear isolators, quasi-zero-stiffness (QZS) systems present a promising alternative. These systems are engineered to attain a state of close to zero-stiffness by aligning positive and negative stiffness components in a parallel configuration [5,6]. The design principle allows for the neutralization of one stiffness type by the other, aiming for a combined effect that approaches zero-stiffness, as shown in Fig. 1(a). This unique combination is achieved through the alignment of positive stiffness elements, such as coil springs, which exhibit a linear response, with negative stiffness mechanisms, such as buckling beams, that display fundamentally nonlinear behavior. Although overall zero-stiffness is not sought after, as this would lead to an unstable system, QZS systems exploit their nonlinear nature to create a state where zero-stiffness is flanked by regions of positive stiffness, providing stability [7,8]. This results in high static stiffness necessary for supporting large static loads, while maintaining low dynamic stiffness to extend the frequency range of effective isolation towards lower frequencies.

The landscape of QZS system designs includes both passive and active configurations [6,8]. Passive QZS systems use fixed mechanical setups tailored to specific applications, typically optimized for isolating a single load within a narrow displacement range. Although some designs can adapt to varying loads [9–13], these are predominantly active systems. Active QZS systems employ closed-loop control to adjust dynamically to load changes, offering greater versatility but at the cost of added complexity, as they require sensors, actuators, and control algorithms. While both passive and active QZS systems achieve effective vibration isolation, their load sensitivity, and, for active systems, complex design emphasize the need for a passive vibration isolation solution that can maintain zero-stiffness across a wide displacement range and accommodate varying loads.

1.2. Pneumatic isolators

Industrially available pneumatic cylinders offer a potential solution for achieving low stiffness passively across varying loads. By attaching a large external volume relative to the cylinder's internal volume, these actuators can approximate zero-stiffness, yielding a nearly constant-force characteristic. However, they are unsuitable for low-frequency vibration isolation due to the stick-slip effect caused by changing friction between the sealing ring and cylinder wall [14]. This effect leads to erratic motion, especially at low frequencies, disrupting the constant-force characteristic, as shown in Fig. 1(b).

To address the stick-slip effect in pneumatic cylinders, several options exist. Advanced piston-cylinder configurations employing hydrostatic air bushings to support the cylinder rod offer extremely low friction but require a continuous air supply, making them unsuitable for passive operation [15]. Alternatively, the piston seal is replaced with a flexible membrane [1], which can take various forms, including flat, bellow, or rolling-lobe. However, all membrane types inherently introduce additional stiffness, which complicates achieving the desired zero-stiffness characteristic (Fig. 1(c)). Flat membranes, often used in vibration isolation tables [16], provide minimal stiffness due to small membrane deformations at large volumes and low pressures, which in turn hinders compact designs. Bellow-type membranes, while much more compact, tend to exhibit significant stiffness due to undesirable increases in effective area during loading [17]. While rolling membranes also show such behavior, the membrane stiffness can be counteracted with additional design features. Thus, truly passive operation with minimized friction in a compact form factor is most effectively achieved using rolling membrane designs.

Rolling-lobe air spring vibration isolators achieve zero-stiffness by balancing positive and negative stiffness. In principle, this is similar to QZS systems, but achieved through different mechanisms. Rolling-lobe vibration isolators operate using a flexible membrane that rolls over a piston as the isolator is displaced. Negative stiffness arises from changes in the effective area during this motion, achieved by guiding the flexible membrane through piston and external guide geometry. Notably, this negative stiffness can be achieved over the entire displacement range of the air spring unlike in QZS systems. By combining the area-based negative stiffness with the positive stiffness of the membrane and the compressible gas, rolling-lobe air springs can be engineered to closely approximate zero-stiffness overall.

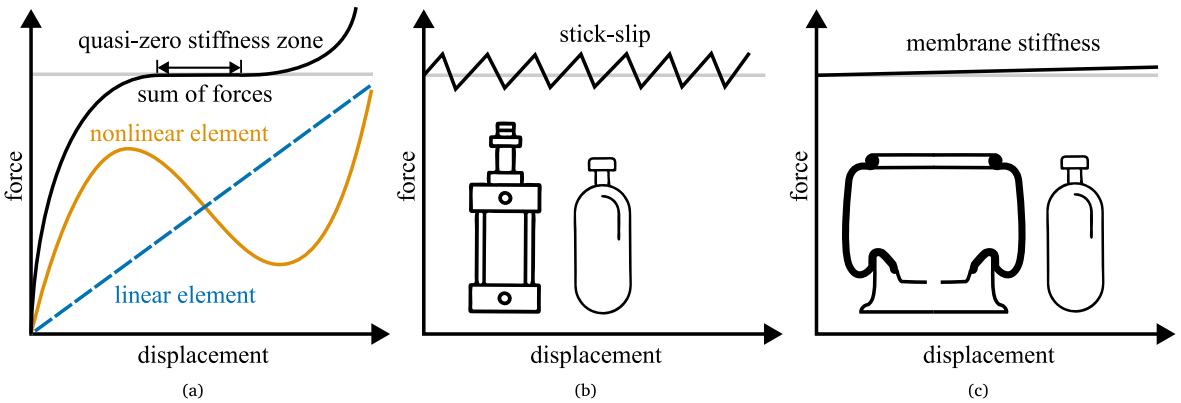

Fig. 1. Force-displacement curves of different passive zero-stiffness approaches: QZS (a), pneumatic cylinder with external volume (b) and rolling-lobe air spring with external volume (c). The horizontal gray line displays the ideal zero-stiffness property.

1.3. Objective of this paper

This paper demonstrates how rolling-lobe air springs can be adjusted for low-frequency vibration isolation through the strategic balance of their positive and negative stiffness elements. By analyzing each component affecting stiffness, namely the gas spring, membrane behavior and geometry of the external guide and piston, this study reveals how these elements can be tailored to achieve zero-stiffness over a wide displacement range and for varying loads. Through a combination of theoretical analysis, experimental testing, and modeling, the paper establishes practical design guidelines that make rolling-lobe air springs a viable alternative to state-of-the-art QZS isolators, overcoming limitations in load adaptability and effective isolation displacement range. The results provide insights for the development of adaptable, high-performance rolling-lobe isolators that enable passive, zero-stiffness operation for low-frequency vibration isolation.

The main contributions of this paper to the existing literature on vibration isolation systems are as follows:

1. Explicit derivation of rolling-lobe stiffness terms, highlighting positive and negative elements that align with QZS isolators.
2. Systematic exploration of how isolator configuration changes impact nonlinear stiffness, damping, and overall isolation performance.
3. Provision of design guidelines for achieving zero-stiffness over a large displacement range with load adaptability.
4. Modeling of experimental rolling-lobe isolator behavior using a Duffing oscillator model.
5. Demonstration of practical manufacturability using 3D-printing for customized isolator designs.

The remainder of this paper is structured as follows: In Section 2, the theoretical principles underlying the behavior of ideal air springs are outlined, providing a foundation for understanding their performance characteristics. This is followed by a detailed account of the design and fabrication process of 3D-printed air springs in Section 3, where design considerations and geometric optimizations are discussed. The methodology used to assess the performance of these 3D-printed rolling-lobe isolators is then presented in Section 4, covering both experimental setups and analytical approaches. The results of these approaches are analyzed in Section 5, focusing on modeling the actuator and its vibration isolation capabilities. A discussion of the implications of these findings along with gathered design guidelines is provided in Section 6. Finally, the paper concludes with an overview of the key outcomes and suggests avenues for future research in Section 7.

2. Theory of ideal air springs

To understand rolling-lobe isolator behavior and achieve zero-stiffness, it is essential to begin with an idealized model of air springs. This model clarifies the fundamental control mechanisms necessary for zero-stiffness. In this context, the membrane's stiffness, geometry and gas dynamics are investigated to maintain zero-stiffness across various load cases.

In an idealized model, the total stiffness k_t of an air spring arises from two primary components: the stiffness of the gas spring k_g and the stiffness of the membrane k_m. These contributions sum up to determine the overall stiffness k_t, as expressed by

$$k_t = k_g + k_m \,. \tag{1}$$

For a zero-stiffness air spring design, k_t has to be zero. This requires that the negative stiffness component introduced by the gas spring precisely counterbalances the positive stiffness contributed by the membrane.

Determining the factors influencing the gas spring stiffness k_g necessarily begins by looking at the force F exerted by the gas spring

$$F = p \cdot A \,. \tag{2}$$

Here, p is the pressure in the system, and A is the area on which the pressure acts. Both p and A are functions of the displacement z, making the force dependent on the spring's displacement. The stiffness of the gas spring is derived by differentiating Eq. (2) with respect to the displacement z

$$k_g = \frac{\mathrm{d}F}{\mathrm{d}z} = \frac{\mathrm{d}p}{\mathrm{d}z} A(z) + \frac{\mathrm{d}A}{\mathrm{d}z} p(z) \,. \tag{3}$$

If solving above equation for the spring geometry $\frac{\mathrm{d}A}{\mathrm{d}z}$, an expression for the change in pressure $\frac{\mathrm{d}p}{\mathrm{d}z}$ is needed. Here, the ideal gas law

$$pV^n = \text{const.} \tag{4}$$

is used, where V is the volume and n the polytropic exponent. The polytropic exponent n describes the thermodynamic behavior of the gas, which depends on the excitation frequency. Generally the following behavior can be assumed: quasi-static operation (up to 0.01 Hz) is isothermal, dynamic operation (from 1 Hz and higher) is adiabatic, and intermediate frequencies are described by a polytropic process [18]. In air, the polytropic exponent varies between 1 (isothermal process) and 1.4 (adiabatic process) [19]. Differentiating both sides of Eq. (4) with respect to z yields

$$p \cdot n \frac{\mathrm{d}V}{\mathrm{d}z} + V^n \cdot \frac{\mathrm{d}p}{\mathrm{d}z} = 0 \,. \tag{5}$$

The volume change $\mathrm{d}V$ occurring during a small piston displacement $\mathrm{d}z$ depends on the area

$$\mathrm{d}V = -A(z) \cdot \mathrm{d}z. \tag{6}$$

Substituting Eq. (6) into Eq. (5) and rearranging for $\frac{\mathrm{d}p}{\mathrm{d}z}$ yields

$$\frac{\mathrm{d}p}{\mathrm{d}z} = n\frac{p(z)}{V(z)}A(z)\,. \tag{7}$$

Finally, substituting Eq. (7) into Eq. (3), a formulation for the gas spring stiffness is derived

$$k_g = \frac{n}{V(z)}A(z)^2 + \frac{\mathrm{d}A}{\mathrm{d}z} = k_p + k_A\,, \tag{8}$$

where k_p and k_A are the two components of the gas spring stiffness k_g accounting for the stiffness due to the change in pressure and area, respectively. From Eqs. (6) and (8) a system of differential equations with state variables V and A can be obtained to solve for the spring area $A(z)$ that yields a constant stiffness k_g.

To illustrate the behavior of a zero-stiffness air spring, Eq. (8) is solved for initial conditions of unit pressure, volume, and area under two different polytropic exponents, $n = 1$ and $n = 1.4$. Fig. 2 shows the resulting variations in pressure and area over displacement. The figure highlights that maintaining a constant-force characteristic requires different area adjustments depending on the polytropic exponent. This implies that distinct air spring configurations may be needed for quasi-static ($n = 1$) and dynamic ($n = 1.4$) operation.

Next to the polytropic exponent, the volume V, including the external volume V_{ext}, plays a critical role in determining gas spring stiffness. Larger volumes reduce the pressure change $\frac{\mathrm{d}p}{\mathrm{d}z}$ during displacement, as shown in Eq. (7), thereby decreasing the stiffness contribution k_p. In the same vein, a lower k_p minimizes the required reduction in stiffness k_A through variations in $A(z)$, simplifying the achievement of zero-stiffness. Large external volumes also reduce the spring's sensitivity to changes in the polytropic exponent, helping maintain a near-constant-force characteristic across different excitation frequencies. Therefore, employing a large external volume is beneficial, if not even necessary, in order to achieve zero-stiffness.

Contrary to polytropic exponent and volume, the initial pressure p_0 does not appear in Eq. (8), indicating that the zero-stiffness condition is unaffected by variations in p_0. This in turn enables a single spring geometry to achieve zero-stiffness for different load cases.

In above derivation two key assumptions are made. First, the area $A(z)$ is assumed to follow the geometry of the spring precisely. This ideal behavior requires sufficient internal pressure to ensure that the flexible membrane remains in contact with the piston and external guide contours. Second, the membrane stiffness k_m is assumed to be zero, focusing solely on the gas spring stiffness k_g.

While membrane stiffness is neglected in the idealized model, its influence on overall spring stiffness cannot be ignored in practical designs [20]. Wu et al. [21] provide an analytical approach where membrane stiffness is proportional to the cube of the membrane thickness and inversely proportional to the cube of the lobe radius. Given the complexity of accurately modeling membrane behavior, an experimental approach is chosen to evaluate overall spring stiffness in this study.

To summarize, the ideal model of air springs demonstrates the potential for achieving zero-stiffness by controlling geometry and external volume, assuming constant membrane stiffness. This approach allows for a constant-force output across different load cases. However, practical designs must accurately account for membrane stiffness. Due to the challenges of modeling membrane stiffness, the next sections adopt an experimental approach to evaluate the influence of geometry, external volume, and membrane behavior on overall stiffness and isolation performance of rolling-lobe isolators.

3. Design of 3D-printed vibration isolators

To evaluate the influence of different design parameters on isolation performance, this study designs multiple isolators, which are experimentally investigated. Using 3D-printing to fabricate custom, smaller-scale prototypes enables rapid and cost-effective

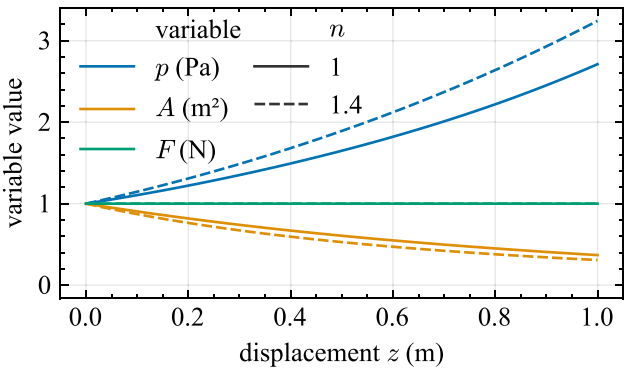

Fig. 2. Pressure, area and force of a zero-stiffness air spring starting with unit pressure, volume and area for different polytropic exponents n.

iteration, as well as easier handling and testing. The flexibility of 3D-printing, already proven effective in developing QZS isolators [22], allows the exploration of complex geometries tailored for improving isolation performance. This section focuses on the design of the rolling-lobe air spring isolator components and their manufacturing.

The 3D-printed isolator, shown in Fig. 3, is an adaptation of industrial rolling-lobe vibration isolators. The isolator consists of a membrane, a base plate, a piston, an external guide and an extension, as illustrated in Fig. 4. The base plate, produced from Grey V4 resin using a Formlabs 3+ stereolithography printer for airtightness, includes an air inlet and a locating feature to center the isolator during testing. The membrane, made from BASF Ultrafuse TPU 95A, is 3D printed on a Prusa MK4 fused filament fabrication printer in vase mode, which involves a single continuous extrusion in a spiral pattern, and is vapor smoothed with tetrahydrofuran for airtightness. The membrane is first attached to the piston with cyanoacrylate adhesive, then turned inside out, and joined to the base plate. Next, the extension cylinder is glued to the piston. Finally, the external guide is pressed onto the base plate. The key dimensions include a maximum membrane diameter of $48\,\mathrm{mm}$, a maximum piston diameter of $40\,\mathrm{mm}$, a membrane thickness of $0.4\,\mathrm{mm}$, and a membrane length of $20\,\mathrm{mm}$ participating in the rolling motion. Additional dimensions are provided in Fig. A.1. A pneumatic fitting with a G $1/8''$ thread is incorporated, with the threads manually cut after the 3D-printing process. In this study, one isolator assembly – consisting of a base plate, piston, and membrane – has been printed, along with three different external guides. By exchanging these guides, three distinct physical isolator configurations are created.

The piston geometry can be adjusted to alter the stiffness of the isolator by changing the effective area throughout the isolator's stroke. In a rolling-lobe air spring, the membrane's diameter decreases from the outer base to the internal piston diameter, resulting in a change in membrane circumference that must fit onto the piston. For a zero-stiffness design, the membrane diameter is larger than the piston diameter, which, if directly translated to circumference, causes the membrane to bunch up at certain points on the piston. This localized bunching reduces the gap between the piston and membrane, leading to higher curvature. Higher curvature increases stress in the membrane and thus is assumed to increase stiffness.

To avoid the issue of the membrane bunching up on the piston, the piston geometry is modified to achieve a larger circumference while maintaining the same cross-sectional area. In its default state, all piston cross sections are circular. These circular cross sections are then modified by superimposing a sine wave onto them. The amplitude $a(z)$ of the sine wave is optimized to yield the same circumference in the piston as in the membrane along the displacement z as shown in Fig. 5. The optimized amplitude is then fitted with a root function which in turn is used to generate the geometry of the piston parametrically. The full derivation of the optimization problem is given in Appendix B.

Along with the piston, the external guide is used to control the effective area of the air spring. In this study, the guide angle s refers to the angle at which the guide opens, as shown in Fig. A.1. A constant opening angle is used, resulting in a linear change in the guide's diameter over displacement z. Although more complex guide designs could be employed for custom stiffness characteristics, this study focuses on guide angles of $0°$ (straight cylinder), $10°$, and $20°$ to gather first insights into the influence of the guide angle on isolation performance.

4. Methods for assessing isolator performance

This section outlines the methodology used to evaluate the performance of 3D-printed rolling-lobe isolators through experimental and theoretical approaches. The main experimental objective is to measure the isolator's stiffness and damping characteristics. Thus,

Fig. 3. Rolling-lobe isolator assembled and depressurized. From left to right: without external guide, with external guide, piston extended.

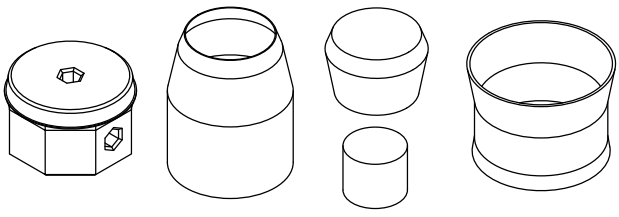

Fig. 4. Individual components of the rolling-lobe isolator. From left to right: base, membrane, piston with extension, external guide.

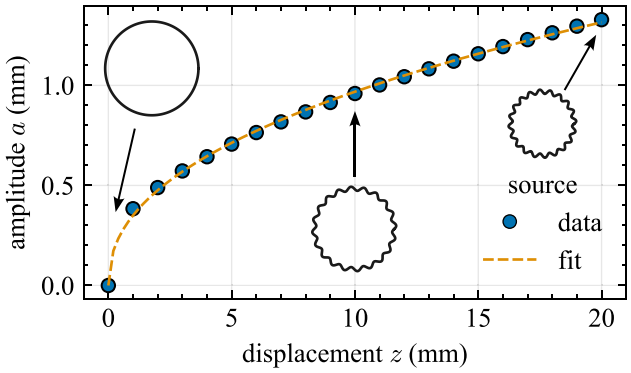

Fig. 5. Optimized amplitude a from parametric Eq. (B.1) to match given piston area and membrane circumference at each displacement z. The data is fitted with a root function. Additionally, the resulting cross sections are shown.

the experimental setup covers the pneumatic system's design, along with the integration of the actuator into a universal testing machine. The experimentally obtained stiffness and damping values are used in mathematical models and simulations to predict and analyze the isolator's vibration isolation performance under various operating conditions. These methods provide the foundation for understanding the isolator's capabilities in practical applications.

4.1. Experimental setup

To operationalize the 3D-printed isolator, a pneumatic system is assembled. The isolator connects to a central tee fitting, which splits the system into two key components: a pressure sensor (Festo SPAN-P10R) monitoring the system's pressure and a pressure tank. The pressure tank is linked to a manual pressure regulator through a valve. This setup allows the regulator to control the system pressure from a pressurized air source, while the valve can isolate the system for passive operation. Airflow is directed through tubing with an outer and inner diameter of 8 mm and 5.5 mm, respectively. The tubing length between isolator and pressure tank is about 30 cm. During pretests, no influence of shorter tubes on the force-displacement curves could be observed. Fig. 6(a) illustrates how these components interact with the isolator.

Once the pneumatic system is set up, the isolator is mounted in the universal testing machine (see Fig. 6(b)) for performance evaluation under sinusoidal excitation. The Zwick HC-25 servohydraulic fatigue testing machine, which can measure forces up to 25 kN, is used for this purpose. The isolator is placed on compression platens: the lower platen, made from solid PLA and 3D-printed, includes a locating pin to ensure proper alignment of the isolator. This platen also rests on the force sensor. The upper platen, made of steel, is attached to the machine's crosshead, completing the setup needed to test the isolator under load.

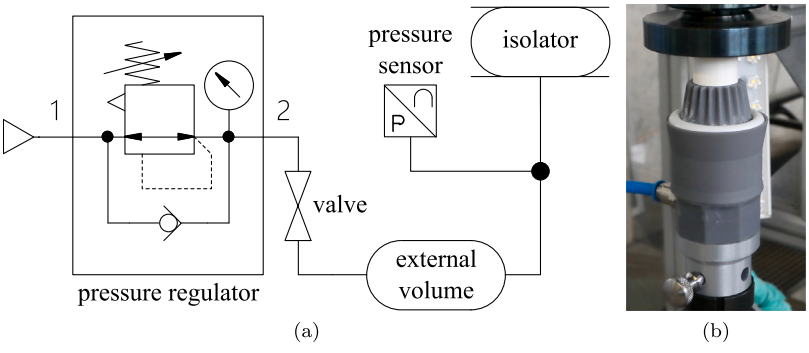

Fig. 6. Experimental setup of the pneumatic circuit (a) and the pressurized isolator mounted in the universal testing machine (b).

Various parameter combinations were tested to assess their impact on the isolator's vibration isolation performance. A full factorial design was used to explore combinations of the following variables:

$$\begin{aligned} \text{amplitude } Z &: \{0.5, 2.5, 5, 10, 15\} \text{ mm} \\ \text{frequency } f &: \{1\} \text{ Hz} \\ \text{pressure } p &: \{1, 2, 3, 4\} \text{ bar} \\ \text{external volume } V_{\text{ext}} &: \{0, 0.75\} \text{ dm}^3 \\ \text{guide angle } s &: \{0, 10, 20\}^\circ \end{aligned}$$

Testing was primarily conducted at an excitation frequency of 1 Hz. This value is considered the lower limit for pneumatic isolators, even for advanced designs [1]. Given that current QZS designs also achieve isolation at this frequency range, it serves as a meaningful benchmark for evaluating isolation performance. Some parameter combinations were not tested due to the risk of rupturing the isolator membrane, particularly at high pressures, large amplitudes and no external volume attached. Additionally, the effect of excitation frequency was examined by testing the parameter combination $p = 3$ bar, $V_{\text{ext}} = 0.75$ dm^3, $s = 10^\circ$ at 0.2, 1.5, 2, 3 Hz and varying amplitudes. Higher frequencies limited the maximum amplitudes due to constraints of the testing machine. Table A.1 lists all the experiments conducted.

The test procedure starts by positioning the unpressurized isolator within the universal testing machine and connecting it to the pneumatic circuit. The force sensor on the testing machine is zeroed. The machine's crosshead is then adjusted so that the isolator's piston is close to, but does not touch, the upper compression platen. Following this, the pressure regulator is used to set the desired pressure level, causing the piston to extend to the upper platen.

Once the isolator is pressurized, the crosshead is moved to the central isolator position, which is designated as the zero relative position for the test. This position is established by bottoming out the unpressurized isolator and then moving the crosshead 17 mm upwards. After reaching the central position, the valve is closed to isolate the system and to ensure no pressure regulation occurs during testing.

With the setup complete, a digital output on the test machine is activated, triggering the recording of pressure sensor data via the HBM QuantumX MX440B data acquisition system. The cyclic loading test then begins, using specified frequency and amplitude values. The test procedure includes 10 ramp-up cycles, during which the amplitude is gradually increased until the target value is reached. The main test consists of 150 cycles (unless noted otherwise) to allow the force-displacement curves to stabilize, indicating that the isolator has adapted to the applied load. After the main test, 10 ramp-down cycles are performed, followed by deactivating the digital output to stop the external pressure measurement.

4.2. Single-degree-of-freedom simulation

Characterizing the isolator's stiffness and damping alone is insufficient for assessing isolation performance. Isolation performance must be evaluated with the isolator supporting a load. The simplest case is a single-degree-of-freedom (SDOF) system, where a mass is coupled to the isolator. In this study, simulations of a SDOF system are used to evaluate isolation performance across different loads and excitation levels, offering a faster approach compared to conducting individual experiments for each case.

There are two situations in which the vibration isolation performance of a SDOF can be assessed. During base excitation, the ground where spring and damper are attached to is displaced under harmonic motion with a given displacement amplitude. The displacement of the mass compared to the displacement of the base describes the transmissibility of external motion into the system. On the other hand, during force excitation, a force of given amplitude is applied to the mass. The transmissibility is now determined by the amplitude of force that is transferred through spring and damper into the rigid base compared to the excitation force amplitude. Both options produce the same results for a linear system [23] but differ for nonlinear ones. In this work, the force transmissibility is chosen as a metric.

For a linear SDOF system under force excitation, the equation of motion is

$$m\ddot{z} + c\dot{z} + k_1 z = F_e \cos(\omega t)\,, \tag{9}$$

where m is the mass, c is the damping coefficient, k_1 is the linear stiffness coefficient, F_e is the force excitation amplitude, and ω is the angular frequency of excitation. The force transmissibility $T(\Omega)$ of such a linear system is given by [24]

$$T(\Omega) = \sqrt{\frac{1 + 4\zeta^2\Omega^2}{(1-\Omega^2)^2 + 4\zeta^2\Omega^2}}\,, \tag{10}$$

where $\zeta = c/(2\,m\omega_n)$, $\omega_n = \sqrt{k_1/m}$, and $\Omega = \omega/\omega_n$.

To accurately capture the nonlinear dynamics of rolling-lobe isolators, a linear model, as represented by Eq. (9), is insufficient. Wu et al. [21] demonstrate that the membrane of a rolling-lobe air spring introduces a significant cubic stiffness contribution, highlighting the need for a model that captures this effect. Consequently, a Duffing oscillator model, which incorporates both linear (k_1) and cubic (k_3) stiffness coefficients, is deemed appropriate for representing the dynamic behavior of a rolling-lobe isolator. This model aligns with the nonlinear characteristics inherent in QZS systems while remaining analytically and computationally tractable, making it a widely adopted approach in the literature [23,25].

The equation of motion for a Duffing oscillator is gained by extending Eq. (9) with the cubic stiffness k_3 [23]

$$m\ddot{z} + c\dot{z} + k_1 z + k_3 z^3 = F_e \cos(\omega t)\,. \tag{11}$$

Normalizing Eq. (11) with respect to m simplifies it to

$$\ddot{z} + \delta\dot{z} + \alpha z + \beta z^3 = \gamma\cos(\omega t)\,, \tag{12}$$

where $\delta = c/m$, $\alpha = k_1/m$, $\beta = k_3/m$, and $\gamma = F_e/m$. Approximating the solution of the steady-state response of the nonlinear system via the first-order harmonic balance method yields [23]

$$(\alpha Z + \frac{3}{4}\beta Z^3 - \omega^2 Z)^2 + (\delta\omega Z)^2 = \gamma^2\,, \tag{13}$$

where Z is the amplitude of steady-state vibration. Due to Eq. (13) being quadratic with regards to ω, solving for same has two solutions:

$$\omega_{1,2} = \left[\left(\alpha + \frac{3}{4}\beta Z^2 - \frac{\delta^2}{2}\right) \pm \frac{1}{Z}\sqrt{\gamma^2 - \delta^2 Z^2\left(\alpha - \frac{\delta^2}{4} + \frac{3}{4}\beta Z^2\right)}\right]^{1/2}. \tag{14}$$

To compute the transmissibility T, the ratio between the transmitted force amplitude F_t and the excitation force amplitude F_e is needed. The mass normalized force $\hat{F}_t$ transmitted into the ground consists of the spring and damping components of Eq. (11)

$$\hat{F}_t = \delta\dot{z} + \alpha z + \beta z^3\,. \tag{15}$$

Applying the first order harmonic balance method to Eq. (15) yields the mass normalized transmitted force amplitude

$$\tilde{F}_t = Z\sqrt{\left(\alpha + \frac{3}{4}\beta Z^2\right)^2 + \delta^2\omega^2}\,. \tag{16}$$

Weighting $\tilde{F}_t$ by the mass normalized excitation amplitude γ gives the force transmissibility

$$T_{1,2} = \frac{\tilde{F}_t}{\gamma} = \frac{Z}{\gamma}\cdot\sqrt{\left(\alpha + \frac{3}{4}\beta Z^2\right)^2 + \delta^2\omega_{1,2}^2}\,. \tag{17}$$

5. Results

In this section, a detailed analysis of the experimental data collected of the isolators under various conditions is presented. The results are organized into several subsections, each representing a step towards developing a simulation model for predicting isolator behavior. An examination of the force-displacement relationships is conducted to understand the effects of different parameter combinations. It is then validated that the large external volume ensures approximately linear pressure behavior. Following this, key parameters, such as stiffness and damping coefficients, are extracted, which are essential for constructing the isolator simulation model. The influence of excitation frequency on these parameters is assessed. Finally, transmissibility is computed using the developed model to evaluate the spring's isolation performance.

5.1. Force-displacement data

The first step in evaluating isolator performance involves examining the raw generated experimental data, specifically the force-displacement curves. Fig. 7 demonstrates that the isolator requires time to settle in, but the force-displacement curves eventually converge. Between 100 and 150 cycles, the changes in the curves are minimal, indicating that the system is approaching a steady state, though minor changes likely continue beyond this point. This behavior is consistent across all tested isolators.

Given the extensive data from 86 individual runs, the force-displacement curves in Fig. 8 illustrate the diverse behavior of the isolator under varying parameter combinations listed in Table A.1. To compare the curves across different parameter combinations, the forces and displacements for each curve have been normalized to lie between −1 and 1, yielding $\hat{F}$ and $\hat{z}$. For example, sample 32

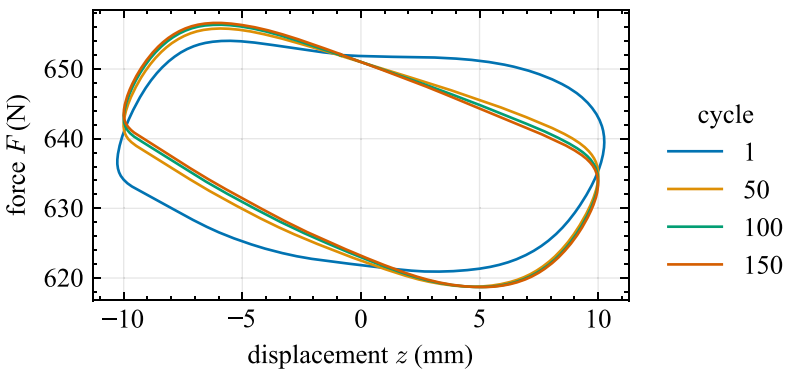

Fig. 7. Force-displacement curves for different cycles of sample 85 ($Z = 10\,\text{mm}$, $p = 4\,\text{bar}$, $s = 10°$, $f = 1\,\text{Hz}$).

($Z = 15\,\text{mm}$, $p = 2\,\text{bar}$, $s = 20°$) demonstrates a pinched curve at negative displacement, leading to predominantly positive stiffness for $z < 0$ and negative stiffness for $z > 0$. This behavior is consistent with other large amplitude samples at pressures equal to or exceeding 2 bar, stemming from the membrane leaving the guide at large negative displacements. In contrast, sample 27 ($Z = 15\,\text{mm}$, $p = 1\,\text{bar}$, $s = 20°$) reveals a meandering curve likely due to insufficient pressure to guide the membrane, a trend also observed at different guide angles and an amplitude $Z = 10\,\text{mm}$. As a comparison, sample 85 ($Z = 10\,\text{mm}$, $p = 4\,\text{bar}$, $s = 10°$) shows a smooth curve with negative stiffness achieved over a large displacement range. Additionally, sample 44 ($Z = 2.5\,\text{mm}$, $p = 3\,\text{bar}$, $s = 10°$) exhibits positive stiffness but very linear behavior, typical for curves where $Z \leq 2.5\,\text{mm}$.

A more general overview is given in Fig. A.2, where the force-displacement curves for all tested isolator configurations at a fixed volume of $V = 0.75\,\text{dm}^3$ and frequency $f = 1\,\text{Hz}$ is shown. The curves reveal several clear trends. Higher internal pressures result in increased forces and enable greater negative stiffness. At higher amplitudes, the curve at negative displacement is pinched, breaking the central symmetry observed at lower amplitudes. Additionally, stiffness decreases with increasing amplitude, as seen in the clockwise rotation of curves at higher amplitudes for the same pressure and shroud angle. Higher shroud angles generate greater forces at the same pressure, likely due to the membrane's increased expansion and the resulting larger effective diameter and thus area of the isolator. Overall, these curves effectively highlight the impact of different parameter combinations on the isolator's performance, showing that both positive and negative stiffnesses can be achieved, thereby indicating the concept's feasibility.

5.2. Pressure data

In addition to force and displacement, pressure data was recorded to gain further insights into the behavior of the isolators. While not of primary interest in modeling isolator behavior, pressure measurements offer valuable information on relative changes in volume and potential flow losses within the tubing. Ideally, with an infinitely large external volume and no flow losses, the pressure would not change at all during the sinusoidal excitation of the isolator. However, this is not achievable in practice and thus the next best case is the pressure following the sinusoidal excitation proportionally, which indicates linear system behavior.

Fig. 9 illustrates the pressure response of an isolator over the time t of one excitation cycle at 1 Hz. This is shown for an isolator configuration with parameters $Z = 10\,\text{mm}$, $p = 2\,\text{bar}$, $s = 10°$ and $f = 1\,\text{Hz}$, comparing cases with and without an attached external volume of $0.75\,\text{dm}^3$ (samples 20 and 57). To indicate linearity, the pressure data is fitted using the sine function

$$p_{\sin} = \mu_1 \sin(2\pi f(t + \mu_2)) + \mu_3, \tag{18}$$

where the parameters μ_1, μ_2, μ_3 and f describe the amplitude, phase shift, pressure offset and frequency of the sinusoidal wave, respectively.

A least squares fitting method was employed to match the recorded measurements. If no external volume is attached, the sinusoidal model underpredicts the maximum pressure and overpredicts the minimum pressure, indicating that the pressure does not vary proportionally with the sinusoidal excitation. In contrast, if the external volume is attached, the sinusoidal fit closely follows the experimental data, indicating linear system behavior. This suggests that the external volume is sufficiently large to prevent non-linear pressure increase and that pressure losses are negligible. It also shows that only by employing the external volume, gas spring stiffness remains low enough for zero-stiffness to be possible, as explained in Section 2. Thus, from here on out, only samples with an external volume attached are investigated.

5.3. Stiffness and damping coefficients extraction

To model isolator behavior as described by Eq. (11), the linear and cubic stiffness coefficients k_1 and k_3 and the viscous damping coefficient c need to be extracted from the experimental data. For the stiffness coefficients k_1 and k_3 parameter extraction is carried out via least squares curve fitting. During curve fitting, the experimental force-displacement data is compared to the force predicted

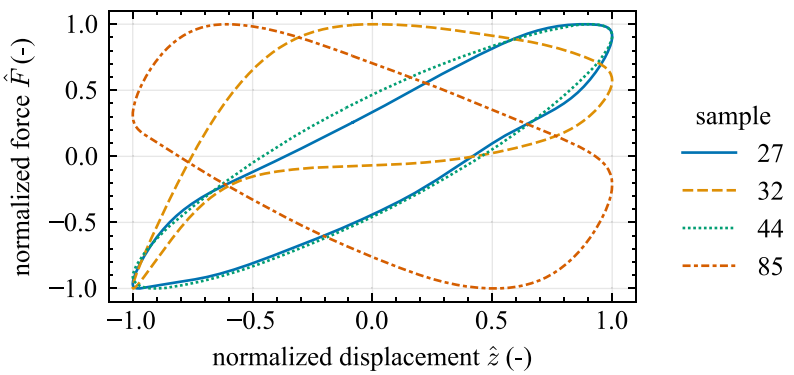

Fig. 8. Force-displacement curves of representative samples of all tested configurations.

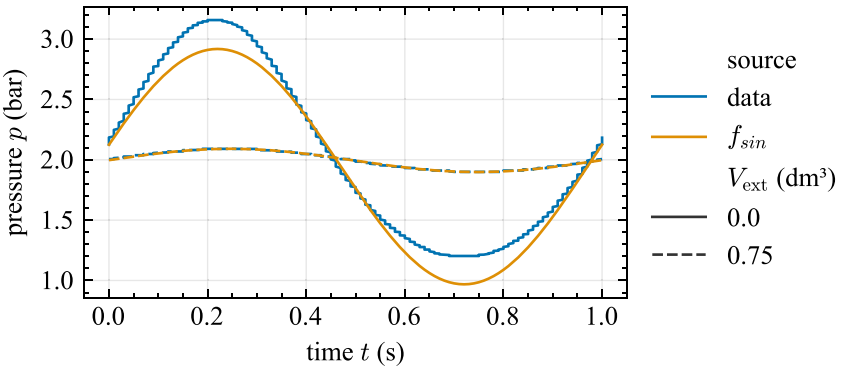

Fig. 9. Pressure over time of one excitation cycle for sample 85 and 57 ($Z = 10\,\text{mm}$, $p = 2\,\text{bar}$, and $s = 10°$) with and without external volume attached.

by the model (Eq. (15)). The viscous damping constant c is determined through optimization to match the enclosed area of the experimental data.

Exemplary for all other samples, the extracted parameters for sample 20 ($Z = 10\,\text{mm}$, $p = 2\,\text{bar}$, $s = 10°$, $f = 1\,\text{Hz}$) are plotted in Fig. 10. This figure shows the experimental data and the curve-fitted model (Eq. (15)). Additionally, the forces resulting from the linear stiffness $k_1 z$, and from the combined linear and cubic stiffness $k_1 z + k_3 z^3$ are plotted individually. Instead of the absolute force F, the relative force $\Delta F = F - \bar{F}_0$ is used, which is obtained by subtracting the mean force $\bar{F}_0$ at $z = 0\,\text{mm}$ from F. As is evident, the experimental data is lacking central symmetry.

The isolator exhibits fundamentally asymmetric force-displacement behavior for designs with a guide angle $s > 0$. Additionally, the membrane may unintentionally exit the guide at large negative displacements, which leads to much more pronounced asymmetries (see sample 32 in Fig. 8). Yet, the used Duffing oscillator model is inherently symmetric. To symmetrize the data, only data where $z > 0$ is chosen because the membrane is always confined by the guide in this case. Using a symmetric model for asymmetric data explains why the fitted curves approximate the isolator's behavior well for $z > 0$ but differ visibly for $z < 0$. This asymmetry is particularly evident when the stiffness nonlinearity is significant, especially at amplitudes $Z > 2.5\,\text{mm}$.

Damping of the isolator is determined by the area enclosed by the force-displacement hysteresis loop. Viscous damping c is determined through optimization, which involves minimizing the difference between the area of the experimental curve for $z > 0$ (shown as the shaded area in Fig. 10) and the simulated system. During this optimization, the values for k_1 and k_3 are arbitrary, as only c influences the enclosed area. Thus, determining the damping coefficient is done before extracting the stiffness coefficients.

The stiffness coefficients k_1 and k_3 are determined using a least squares curve fit method, which leverages many data points for greater accuracy. For amplitudes $Z \leq 2.5\,\text{mm}$, the isolators exhibit mostly linear behavior, making $k_3 \approx 0$. In this case, k_1 is determined using a curve fit where k_3 is set to zero beforehand. This is done to combat the low sensitivity of the fit w.r.t k_3 which would result in physically implausible values otherwise. For larger amplitudes, k_3 is not set to zero beforehand and is determined during the curve fitting process.

Data was extracted in this manner for all experiments, and the individual parameters are compiled in Table A.1. The extracted parameters form the basis for fitting a model that describes individual isolator configurations during operation at different amplitudes.

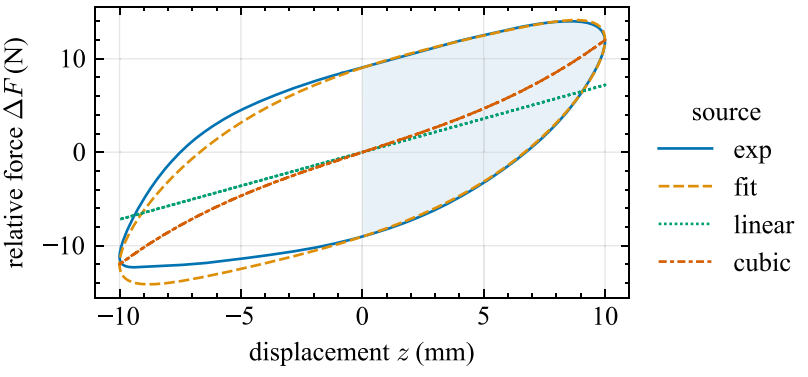

Fig. 10. Experimental curve (exp) and fitted model (fit) with linear and cubic stiffness force for sample 20 ($Z = 10\,\text{mm}$, $p = 2\,\text{bar}$, $s = 10°$). The shaded area is used for damping calculation.

5.4. Isolator model building

Understanding the behavior of the isolator requires knowledge of its stiffness and damping behavior across all operating conditions. In the previous subsection, stiffness and damping coefficient were determined for all tested samples at specific amplitudes Z, guide angles s, pressures p and excitation frequencies f. To extend this understanding to configurations that have not been experimentally tested, a model is developed in this subsection. This model uses the extracted parameters to predict stiffness and damping coefficients for untested amplitudes.

The variation of the linear stiffness coefficient k_1 with amplitude Z is critical in understanding the isolators' behavior. Fig. 11 shows k_1 plotted against Z for different guide angles s and pressures p, where the points represent the extracted values and the lines represent the fitted functions using a least squares regression applied to the following reciprocal function

$$k_1 = \frac{\nu_1}{(Z - \nu_2)} + \nu_3 , \tag{19}$$

where ν_1, ν_2 and ν_3 are the fitted parameters. As Z increases, k_1 decreases monotonically, following a reciprocal relationship. The crossing region refers to the amplitude range where the stiffness curves for different pressures intersect, typically occurring at lower amplitudes for larger s. This region is valuable indicator as the more this region moves towards lower amplitudes, the lower the achievable k_1 at higher amplitudes. Pressure plays a crucial role in influencing k_1, particularly above the crossing region, where higher pressures lead to a more pronounced reduction in k_1, especially for larger s. This behavior confirms the theoretical prediction that a change in effective area, occurring for guide angles $s > 0°$, influences the stiffness of the isolator.

Instead of analyzing k_3 directly, $\hat{k}_3 = k_3 \cdot Z^3$ is used to obtain a curve that more plausibly approaches zero for small amplitudes, which aligns with the physical behavior of the isolator (nonlinearities vanish at small amplitudes) and the assumptions made during parameter extraction. The normalized coefficient $\hat{k}_3$ exhibits an initial rise, and peaks around 10 mm amplitude if $p \leq 2$ bar. While higher pressures generally result in larger $\hat{k}_3$ within each guide angle category, the influence of guide angle on $\hat{k}_3$ remains uncertain due to the lack of consistent correlation. To approximate $\hat{k}_3$ across varying conditions, linear interpolation between data points (Fig. 12) is employed, providing a practical representation for later model building.

Contrasting with the complexity of predicting the cubic stiffness coefficient k_3, the damping coefficient c shows a clear trend with amplitude Z. Generally, c decreases as Z increases, but notably peaks around $Z \approx 2.5$ mm for most curves, especially under higher pressures and larger guide angles. Despite this peak, an overall linear approximation effectively describes the trend of c over Z. This linear model provides a reasonable fit for the majority of data points at different amplitudes. Fig. 13 illustrates this relationship with extracted data points and linear model fits for the three tested guide angles.

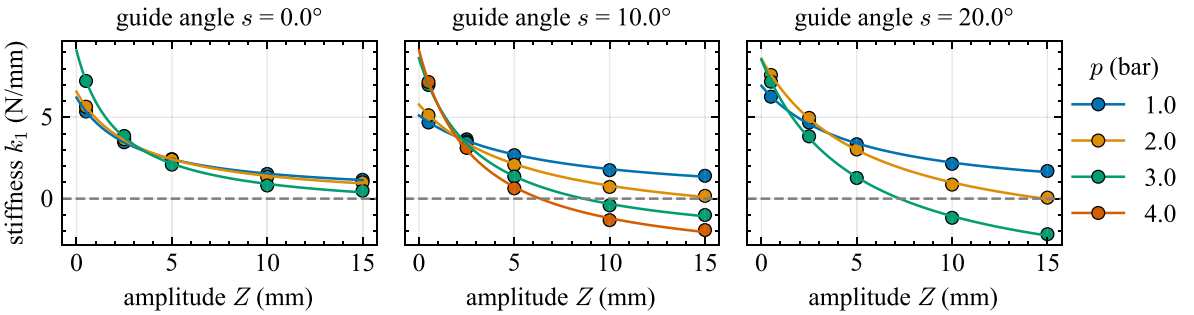

Fig. 11. Fit of linear stiffness coefficient k_1 over amplitude a, markers denote extracted experimental values.

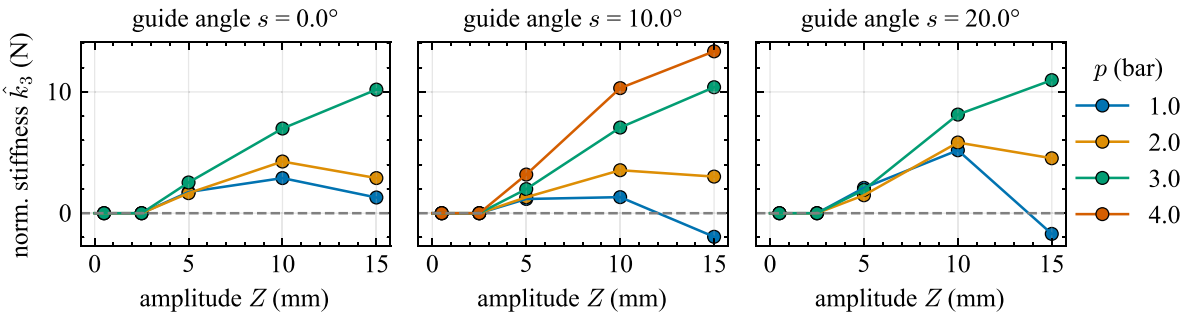

Fig. 12. Fit of normalized cubic stiffness coefficient $\hat{k}_3$, markers denote extracted experimental values.

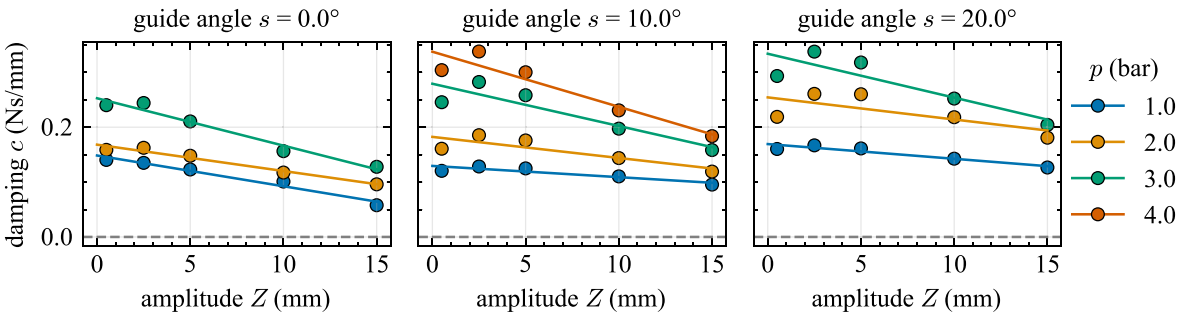

Fig. 13. Fit of viscous damping coefficient c, markers denote extracted experimental values.

5.5. Influence of excitation frequency on extracted parameters

In the experiments using the universal testing machine, multiple excitation frequencies were investigated. However, so far only data from tests conducted at 1 Hz have been presented. To assess the influence of frequency on stiffness and damping coefficients, experiments for one isolator configuration ($s = 10°$, $p = 3$ bar) have been carried out at different excitation frequencies. Three new plots in Fig. 14 compare the prior extracted parameters k_1, $\hat{k}_3$, and c at 1 Hz to the same parameters at differing frequencies. The baseline at 1 Hz is marked with a curve, as in the previous figures, while the data points at frequencies other than 1 Hz are shown only as points.

Frequency exerts minimal influence on k_1, with a slight proportionality observed primarily at lower amplitudes. Significant decreases in $\hat{k}_3$ are evident at higher amplitudes below 1 Hz, while more data points are needed above 1 Hz for a comprehensive assessment. Conversely, c demonstrates a pronounced inverse relationship with frequency, particularly below 1 Hz, where damping increases notably.

5.6. Transmissibility from isolator model

The developed stiffness and damping model is applied to evaluate the transmissibility of the different isolator configurations over a range of excitation frequencies and force amplitudes. The isolator is simulated as part of a single-degree-of-freedom system, as outlined in Section 4.2. First, the transmissibility and displacement amplitude of a single isolator configuration are evaluated to illustrate its isolation performance. Then, the frequency at which isolation initially occurs is determined for all tested configurations, highlighting the impact of the design parameters on isolation effectiveness.

Fig. 15(a) illustrates force transmissibility T over frequency f for the isolator configuration $p = 4$ bar, $s = 10°$. For small excitation force amplitudes, the nonlinear terms vanish, resulting in nearly linear behavior, as shown by the dashed line representing linear transmissibility with k_1 and c extracted from the model for $Z = 0$ mm. As excitation forces increase, amplitudes Z rise, causing

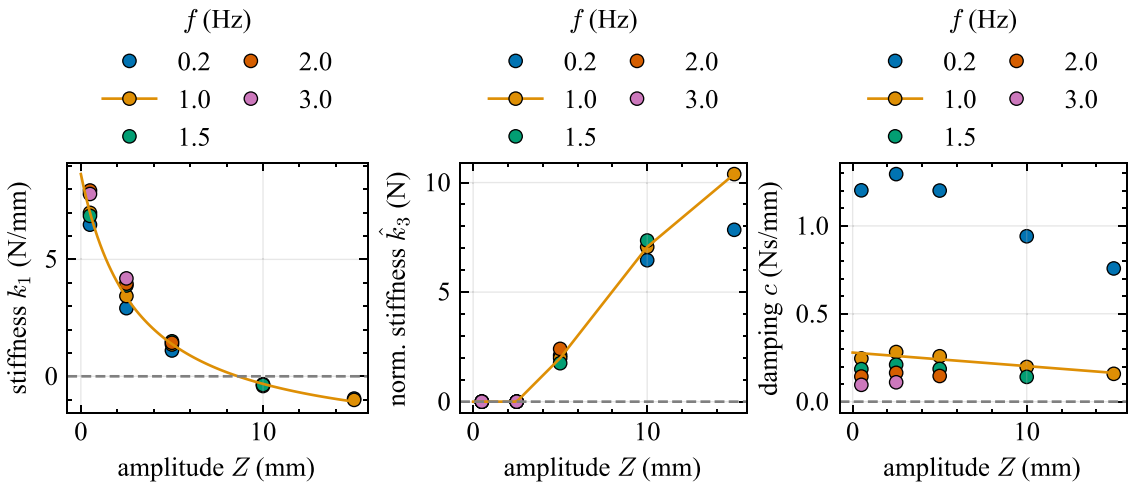

(a) linear stiffness coefficient k_1 (b) normalized cubic stiffness coefficient $\hat{k}_3$ (c) viscous damping coefficient c

Fig. 14. Influence of frequency f on the extracted parameters of the isolator configuration $p = 3$ bar, $s = 10°$.

the isolator to soften, shifting the peak towards lower frequencies and decreasing transmissibility in the resonance region. Further increasing the force amplitude to 10 N eliminates solutions for ω_2 from Eq. (14), while the ω_1 branch extends towards 0 Hz. This results in two observable peaks: a shallow peak near the resonance region of the lower force excitation levels and an inverted peak towards lower frequencies. The shallow peak reaches above $T = 1$ but decreases with further force amplitude increases, whereas the inverted peak grows.

All curves converge at frequencies around 6 Hz, regardless of excitation force amplitude. The transmissibility of the isolators is lower in the resonance region compared to the idealized linear case, but becomes larger from about 3 Hz onwards. Fig. 15(b) shows corresponding displacement amplitude plots, indicating that higher force amplitudes result in higher displacement amplitudes. Generally, these amplitudes remain below 1 mm, except near resonance and a force excitation amplitude of 10 N.

Isolation performance can be evaluated by identifying the frequency f to the right of the resonance peak where $T = 1$ for each excitation force amplitude. Fig. 16 illustrates this extracted frequency across different isolator configurations and force excitation amplitudes, providing a single metric for isolator design. The results generally show a trend of higher pressures and guide angles reducing transmissibility. An exception is observed with the 20° guide angle, which initially shows the highest transmissibility but falls below the values of all other guide angles at $p = 3$ bar, likely due to the membrane not properly contacting the guide at lower pressures.

6. Discussion

The results offer valuable insights on isolator behavior but require a closer examination to assess their implications. This discussion focuses on evaluating the experimental data quality, as well as the accuracy of the stiffness, damping, and transmissibility models. Understanding these aspects helps to inform practical design guidelines for optimizing rolling-lobe isolators in low-frequency vibration isolation applications.

6.1. Experimental data quality and measurement consistency

The experiments generated data of high resolution, allowing for detailed measurements of force and displacement. This level of detail is crucial for capturing the nuances of isolator behavior, particularly at small amplitudes. Specifically, the force resolution

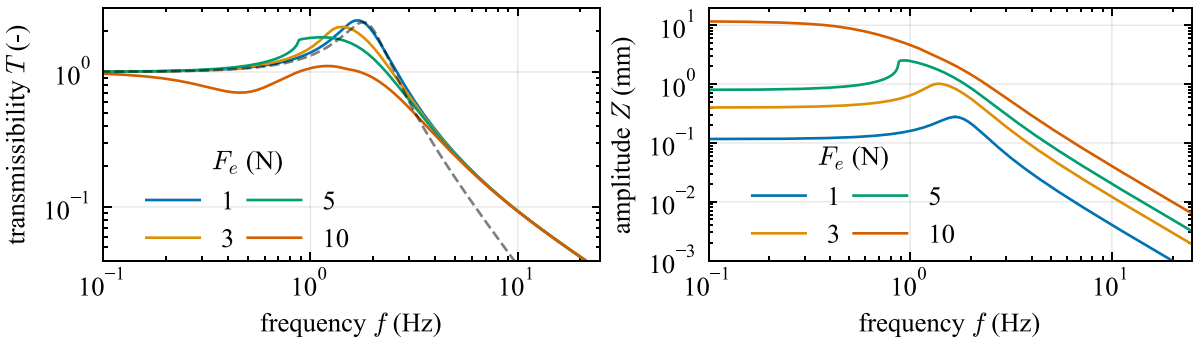

(a) force transmissibility (b) displacement amplitude

Fig. 15. Force transmissibility T and amplitude Z over frequency f for different excitation levels F_e of the isolator configuration $p = 4$ bar, $s = 10°$.

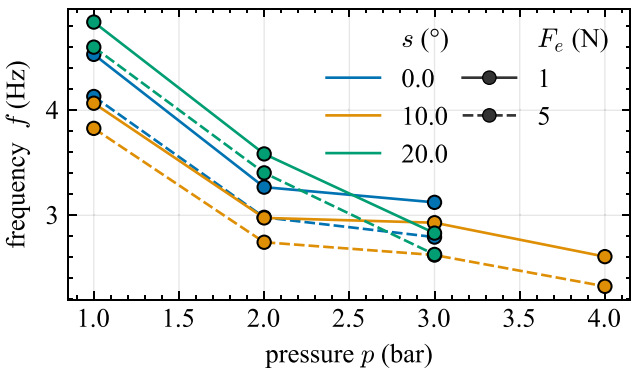

Fig. 16. Extracted Frequency f at $T = 1$ for different combinations of pressures p and guide angles s and force excitation amplitudes F_e. Lines connecting data points are drawn for enhanced visual clarity not valid data interpolation.

was below 0.1 N, which proved adequate for all tests conducted. However, at small amplitudes, the minimal overall change in force led to stairstepping effects in the data. These effects were mitigated by applying a least squares fit to accurately determine the coefficients taking all the data into account.

For the testing of each isolator the starting conditions have to remain comparable. After changing isolator configurations, manual repositioning of the universal test machine's crosshead to the central isolator position was required. The accuracy of this operation was limited to 0.1 mm. Additionally, uncertainties in internal pressure measurements (±0.15 bar resolution) influenced the effective starting area due to pressure induced membrane deformation. Since the guide angle of the tested isolator is constant and the extracted parameters depended on the relative change in force, small shifts impacting the starting conditions are assumed to have had minimal impact.

6.2. Isolator model validity

The displacement amplitudes in the design of experiments were selected based on their potential to achieve overall zero-stiffness, thus placing less emphasis on smaller amplitudes. However, outside the resonance region, the transmissibility model indicates that displacement amplitudes are much lower than those investigated experimentally. This discrepancy increases the model's reliance on accurately predicting stiffness and damping at small amplitudes, potentially reducing prediction accuracy. This primarily affects the estimates of linear stiffness k_1 and damping c coefficients at low amplitudes. Their general impact on transmissibility is discussed in the next subsection.

Additionally, internal pressures $p \leq 3\,\mathrm{bar}$ can prevent the membrane from following the intended guide geometry at guide angles $s \geq 0°$. This results in mislabeled data, where different configurations are incorrectly grouped under a single guide angle. This mislabeling explains the wider crossing region of pressure curves at a guide angle of $s = 20°$ in Fig. 11. Although this affects the accuracy of isolation performance predictions for these specific configurations, the higher-pressure configurations, which show better isolation performance, remain unaffected.

Modeling the linear stiffness behavior of rolling-lobe air springs over displacement amplitude using a reciprocal function is well established in the literature [18,21]. However, this approach addresses only the linear stiffness component of the model. The higher order cubic stiffness term, required in the Duffing oscillator model, is more challenging to model, particularly since this aspect remains unexplored in the existing literature on rolling-lobe isolators.

Another restriction associated with the Duffing oscillator model is its assumption of central symmetry in the isolator's behavior. Yet, in practice, the isolator exhibits inherent asymmetry at non-zero guide angles. This asymmetry primarily arises from the changing piston and external guide diameter with displacement, which introduces a quadratic influence on the force ($F = p \cdot A \propto p \cdot d^2$). Consequently, the model's assumption of a purely cubic non-linear stiffness is insufficient to capture the full behavior of the system, especially at larger amplitudes where asymmetry becomes more pronounced.

To enforce the model's symmetry requirement, only one side of the force-displacement data is used during model fitting. This approach leads to noticeable differences between the model and experimental data at larger amplitudes, where the effects of asymmetry are more significant. Nonetheless, the model provides reliable predictions for the positive displacement across all tested amplitudes. For larger amplitudes, where asymmetry significantly influences behavior, an updated model that accounts for the quadratic influence could enhance predictive accuracy.

In summary, future work could explore advanced isolator modeling to better capture the isolator's asymmetric dynamics. Furthermore, optimizing the isolator's design to reduce asymmetry may simplify modeling and improve the Duffing oscillator's predictive accuracy. While the current Duffing model serves as a practical baseline for analyzing the isolator's performance under low-asymmetry conditions, extensions are required to account for asymmetric effects at larger amplitudes. Notably, refining the isolator's design through the parameters outlined in Section 2 could inherently mitigate asymmetry, thereby enhancing the predictive capability of the already employed Duffing oscillator model.

6.3. Transmissibility model validity

As the transmissibility model is based on the predictions generated by the isolator model, it also inherits its limitations. The transmissibility curves are thus primarily influenced by the isolator model, which is experimentally validated at higher amplitudes and a fixed frequency of 1 Hz. Although these validations increase confidence in the model at these specific conditions, the model's accuracy at smaller amplitudes and differing frequencies remains untested due to limited experimental data. While the effect of frequency is considered less significant than that of amplitude, the model does not currently account for it.

A frequency-dependent model would generally alter the transmissibility curve in both directions from the fixed frequency measurements taken at 1 Hz. Below 1 Hz, increased damping and reduced linear stiffness lead to a more gradual decline in transmissibility and lower the frequency at which isolation begins. Above 1 Hz, decreased damping results in a sharper drop in transmissibility, while increased linear stiffness raises transmissibility overall. These trends suggest lower transmissibility with slower decay in the sub-1 Hz range, and higher transmissibility with a faster decline above 1 Hz. Additionally, reduced cubic stiffness below 1 Hz produces less tilted resonance peaks, indicating reduced isolator softening, while a slight increase in cubic stiffness above 1 Hz leads to more tilted peaks in that range.

Under certain excitation conditions, the model may predict nonphysical behavior. This is illustrated by the negative transmissibility peak observed in Fig. 15(a) at an excitation force amplitude of 10 N. Since the force amplitudes remain within the model's valid range [23], this negative peak reflects system instability caused by the linear stiffness coefficient k_1 becoming negative due

to isolator softening at large amplitudes. Notably, the displacement amplitudes at the negative peak align with those where k_1 first turns negative. In reality, this condition would cause system vibration to cease, but the model does not predict this outcome, resulting instead in implausible behavior. These nonphysical results from the harmonic balance method highlight the importance of carefully considering the data used to build the model.

To achieve more accurate predictions that can actively inform the isolator design process, several options can improve upon the current model. The most straightforward approach is to expand the experimental dataset by collecting more data across a broader frequency and amplitude range. Additional data points at frequencies below 1 Hz would better capture damping behavior, while extending data collection above 1 Hz would refine predictions for cubic stiffness.

Another method to improve the accuracy of transmissibility measurements involves experimentally exciting an SDOF system, comprising the isolator and its load, with a shaker. Excitation can be either harmonic at discrete frequencies or employ a swept-sine excitation over a continuous frequency range. This data can be directly used to generate transmissibility curves without relying on model-based calculations. Additionally, a swept-sine approach provides insights into the transient behavior of the isolator. Such methods offer two key advantages: higher-fidelity transmissibility data that directly inform design decisions, as demonstrated by Lee and Kim [26], and the ability to capture higher harmonics and asymmetric behaviors [27], both of which significantly influence vibration isolation performance. Despite these advantages, a shaker-based setup introduces considerable complexity, particularly when working with variable loads. Achieving the required static load often necessitates either a large mass or a second actuator. Supporting large masses requires a stabilizing fixture, which can impact measurement accuracy. Employing a second actuator in a tandem configuration adds further complexity and assumes the availability of a second actuator of the same type [18]. As a result, the experimental approach adopted in this work – characterizing stiffness and damping and simulating transmissibility using analytical models – remains a widely used methodology for evaluating QZS isolators [12,28,29].

Next to physical experiments, finite element simulations offer a viable addition. They enable predictions of stiffness and damping trends across amplitude and frequency ranges that may be challenging to capture experimentally. While simulations can operate independently, combining them with experimental data for validation strengthens model accuracy. With a finite element model, the entire isolator system can be optimized virtually, allowing adjustments to parameters like membrane stiffness [20,21] or external volume to achieve specific performance goals, such as zero-stiffness across different operating ranges. Thus it appears beneficial to include simulation tools if obtaining specific isolator properties is desired.

6.4. Factors driving vibration isolation performance

Following the evaluation of data and model validity, the focus shifts to identifying the parameters that most significantly impact rolling-lobe air spring isolation performance. Which factors shape effective isolation, and how can these insights inform the design of rolling air springs for low-frequency applications? This analysis centers on the adjustable isolator parameters, such as geometry, size of external volumes and membrane behavior due to internal pressure influence, while also considering given external conditions, including excitation frequencies, amplitudes, and the role of transient vibrations.

The primary geometric feature influencing the stiffness of the rolling-lobe air spring is the external guide, which introduces a source of negative stiffness to the spring's design. This feature is central to achieving overall zero or even negative stiffness, with stronger negative stiffness effects generally resulting from higher guide angles s. However, this effect relies on the assumption that the membrane consistently deforms to remain in contact with the guide, which may not always occur, as observed at $s = 20°$ under pressures below 2 bar. This indicates that the change in guide radius must be carefully managed to stay within feasible limits. This constraint limits the maximum achievable negative stiffness, underscoring the importance of complementary mechanisms increasing the magnitude of negative stiffness while decreasing positive stiffness at the same time.

In addition to the external guide, the piston geometry offers another adjustable parameter. In this study, the piston is primarily contoured to guide membrane deformation, although it can also influence overall stiffness. Visual observations during testing indicate that the membrane closely follows the piston contour, effectively eliminating localized bunching. This design likely contributes to a more uniform strain distribution across the membrane, which could reduce the isolator's positive stiffness. Moreover, similar to the external guide, the piston geometry can alter the effective cross-sectional area of the spring, further reducing its negative stiffness component. Although this effect is less pronounced due to the piston's smaller cross-section, it avoids the contact limitations associated with the external guide. Optimizing piston geometry to reduce stiffness may allow for a smaller external guide angle, thus minimizing contact issues there and enhancing overall performance. In this way, the piston shape influences both positive stiffness by improving membrane strain distribution and negative stiffness through area adjustments.

The positive stiffness of the isolator is mainly influenced by two factors: the stiffness of the gas inside the isolator and the stiffness of the membrane. The membrane's material TPU exhibits three distinct characteristics: non-linear hyperelasticity, time dependence and softening during cyclic loading [30]. Thus the membrane's stiffness heavily depends its deformation state and history, which in turn is affected by internal pressure and vibration amplitude. Since vibration amplitude cannot be controlled through design, only the internal pressure can be adjusted. Higher pressures lead to increased stress in the membrane, in turn reducing membrane stiffness due to non-linear stress-strain behavior [30]. Thus, higher pressures enable more compact designs of the same load bearing capability with improved isolation performance.

Additionally, the cyclic softening property of the membrane material introduces a conditioning period before the isolator reaches steady-state isolation performance. This conditioning means the isolator requires a certain number of cycles to stabilize, as illustrated in Fig. 7. Any sudden changes in vibration amplitude or frequency could restart this conditioning process, affecting the isolator's

immediate effectiveness in applications with varying vibration frequencies and amplitudes. For this reason, steady-state operation is preferred with this type of isolator to ensure consistent performance.

In rare cases, membrane rupture caused the isolator to cease operation, typically occurring at high internal pressure, large amplitudes and without an external volume attached. While such conditions do not achieve zero-stiffness and are less relevant for vibration isolation, they underscore the importance of properly sizing both the membrane and the external guide. Membrane rupture was usually preceded by external guide failure, which allowed the membrane to expand uncontrollably and exceed its allowable stress. Reinforcing the external guide, such as by increasing wall thickness, prevents membrane rupture without altering isolator properties. Additionally, membrane thickness must be carefully selected to balance low stiffness and reliability. A conservative estimate for membrane stress can be obtained by modeling the membrane as a 180° cylindrical arc under tangential stress $\sigma_t = \frac{pR}{t}$, where p is the internal pressure, R is the local radius of curvature, and t is the membrane thickness. This formula is equivalent to the hoop stress formula of a thin-walled cylindrical pressure vessel [31]. Ensuring σ_t remains below the allowable stress under peak operating conditions allows for thinner membranes to reduce stiffness while mitigating rupture risks. In the tested isolator configurations, σ_t remained well below the membrane's ultimate strength, confirming that rupture occurred due to external guide failure.

Reducing the positive stiffness of the gas inside the isolator is achieved by attaching an external volume to the isolator, as shown theoretically in Section 2. This reduction in gas spring stiffness is independent of internal pressure, maintaining its effect consistently across various supported loads. Consequently, adjusting the external volume provides a reliable means to counteract the variable membrane stiffness, which changes with internal pressure, vibration amplitude, and frequency. By tuning the external volume, the overall isolator stiffness can be brought back to zero, balancing out the membrane's changing stiffness under different operating conditions. This capability enables a single isolator design with fixed geometry to support multiple load scenarios while achieving zero-stiffness. Although experimental adjustments to the external volume were not made with the goal of reaching zero-stiffness, the results support the theoretical relationship between external volume and stiffness modification.

To design a rolling-lobe air spring optimized for low-frequency vibration isolation, certain principles should be followed. First, incorporating an external guide is essential to introduce the necessary negative stiffness. To mitigate contact issues between the membrane and external guide, the piston geometry should also contribute to producing negative stiffness, thereby reducing the required guide angle on the external guide. Minimizing the system's positive stiffness components helps reduce the required negative stiffness, which in turn decreases the external guide angle and piston contouring needed, alleviating contact issues and asymmetric isolator behavior. To lower membrane stiffness, a high-pressure, compact design is recommended. Adding an external volume reduces gas stiffness, linearizes spring behavior, and thus prevents the introduction of higher harmonics during vibration isolation. Therefore, a large external volume is beneficial. Otherwise, a trade-off between volume size and isolation performance may be necessary to achieve optimal results.

6.5. Comparison with existing QZS isolators

Comparing the rolling-lobe isolator design with other passive QZS isolators presented in the literature is challenging, as isolation performance metrics are not always reported. Consequently, this comparison is limited to studies that provide transmissibility data and use experimental methods to derive these metrics, either directly or indirectly.

For instance, Shuai et al. [12] employ multiple commercial bellow-type air springs in a QZS configuration to isolate a 1000 kg mass from vibrations starting at approximately 1.5 Hz. Similarly, Shi et al. [13] use multiple air springs in a QZS arrangement to achieve isolation from 2 Hz and higher of a 60 kg mass. Vo et al. [28] combine an air spring with a wedge-and-roller cam mechanism to isolate a 4.7 kg mass beginning at 0.3 Hz. In contrast, Wang et al. [32] and Kim et al. [29] utilize purely mechanical systems, achieving isolation at approximately 2.5 Hz for a 10 kg mass and 2 Hz for a 0.76 kg mass, respectively.

These findings show that the rolling-lobe isolator, which achieves isolation from approximately 3 Hz and supports masses ranging from 15 kg to 65 kg, operates in the same frequency range as other passive QZS systems. Moreover, it accommodates vibration amplitudes of up to 15 mm - significantly higher than those reported in comparable literature. Furthermore, pneumatic isolators (as highlighted in this work and in other's [12,13]) excel at isolating larger loads due to their higher force density compared to mechanical springs while being adaptable to varying loads.

6.6. Cost and scalability considerations

While this study relies on 3D-printing to produce multiple prototype isolators efficiently, the same geometrical concepts can be scaled up or transferred to more conventional manufacturing processes. Industrial processes such as injection molding and rubber vulcanization are commonly employed for high-volume air spring manufacturing, making them economically viable for large-scale commercial applications. These methods can accommodate the intricate piston geometries proposed in this study without significant cost penalties, especially once tooling is established. By contrast, for specialized or low-volume runs, the flexibility of 3D-printing may remain appealing, as it eliminates expensive tooling and enables rapid design iterations. Notably, the same printing technology used in this study can scale the isolator up by an order of magnitude in dimension, enabling approximately two orders of magnitude higher load-bearing capacity. Consequently, cost considerations depend largely on production volume, part complexity, and customization needs, rather than on any inherent limitation of the rolling-lobe isolator concept itself.

7. Conclusion

This study explores the design and performance of rolling-lobe air springs in the context of vibration isolation. The herein presented air springs are passive vibration isolators, composed of few parts. These parts are fabricated using 3D-printing allowing for precise control over the isolators' geometry while enabling rapid prototyping. The isolators' performance is evaluated through experimental testing under harmonic excitation at various amplitudes and frequencies. Data is collected for a range of isolator configurations, differing in geometry and applied internal pressure. The force-displacement data obtained from these experiments serves as the basis for developing a predictive isolator model capable of evaluating isolator behavior across a range of excitation amplitudes and frequencies.

Using this model, rolling-lobe air spring vibration isolation performance is assessed, with force transmissibility serving as the key metric. The results indicate a strong influence of isolator geometry, internal pressure and excitation amplitude on the isolation performance. Out of all tested parameter combinations, the most promising isolator configuration achieves effective isolation from close to 2 Hz onwards.

This study has demonstrated distinct advantages of rolling-lobe isolators. Rolling-lobe isolators can achieve zero or even negative stiffness within a vibration isolation context. Unlike QZS systems, the rolling-lobe air spring operates as a single unit, reducing the number of components and simplifying construction. Additionally, its load-bearing capability can be adjusted by altering the internal pressure, offering flexibility in its application while still enabling passive operation. The results show that the isolator's stiffness can be tuned by modifying its geometry, allowing for the potential of zero-stiffness across a large displacement range. Due to the membrane material TPU exhibiting non-linear hyperelastic behavior, large amplitude operation positively impacts the air springs' ability in achieving zero-stiffness.

The findings also reveal that next to amplitude, the membrane's behavior is additionally influenced by internal pressure. Contrary to the idealized theory of air spring behavior where stiffness is pressure-independent, the experiments uncover that higher internal pressures lead to a reduction in stiffness. This effect is caused by the non-linear hyperelasticity of TPU. Additionally, TPU's cyclic softening property introduces a conditioning period necessary for the isolator to reach steady-state performance. This conditioning implies that isolation performance might need several cycles to be fully realized.

Overall, the rolling-lobe air spring remains a promising vibration isolator design, characterized by its simplicity in construction, passive operation, and high tunability – features, which are sought after in mounting solutions for transport and industrial machinery. These findings pave the way for designing an isolator that achieves true zero-stiffness across varied load cases and displacements, for refining performance through high-pressure configurations, and for targeting applications with steady-state isolation needs to fully leverage the isolators' conditioning characteristics.

CRediT authorship contribution statement

Moritz Sprengholz: Writing – review & editing, Writing – original draft, Visualization, Validation, Software, Resources, Methodology, Investigation, Formal analysis, Data curation, Conceptualization. **Christian Hühne:** Writing – review & editing, Supervision, Resources, Project administration, Funding acquisition.

Declaration of Generative AI and AI-assisted technologies in the writing process

During the preparation of this work the authors used ChatGPT by OpenAI in order to improve the readability and structure of already drafted text. After using this tool, the authors reviewed and edited the content as needed and take full responsibility for the content of the published article.

Declaration of competing interest

The authors declare that they have no known competing financial interests or personal relationships that could have appeared to influence the work reported in this paper.

Acknowledgments

This research was funded by the German Federal Ministry for Economic Affairs and Climate Action (BMWK) under project number 20A2103D (MuStHaF). We would also like to thank Patrick Meyer for his invaluable assistance in proofreading the initial draft of this paper.

Appendix A. Figures and tables

Table A.1
Overview of all tested samples.

Sample	Z mm	f Hz	p bar	V dm^3	s °	k_1 N/mm	k_3 N/mm^3	c Ns/mm	$\bar{F}_0$ N
2	0.5	1	1	0.75	0	5.3588	0	0.1404	142.0
3	2.5	1	1	0.75	0	3.4698	0	0.1350	143.4
4	5	1	1	0.75	0	2.4338	0.014	0.1230	143.9
5	10	1	1	0.75	0	1.5209	0.0029	0.1010	144.7
1	15	1	1	0.75	0	1.1562	0.0004	0.0578	144.1
12	0.5	1	1	0.75	10	4.6871	0	0.1205	147.6
13	2.5	1	1	0.75	10	3.6474	0	0.1284	148.2
14	5	1	1	0.75	10	2.6746	0.0094	0.1249	148.6
15	10	1	1	0.75	10	1.7506	0.0013	0.1104	149.2
16	15	1	1	0.75	10	1.4046	−0.0006	0.0954	150.1
22	0.5	1	1	0.75	20	6.2720	0	0.1603	142.7
23	0.5	1	1	0.75	20	6.2720	0	0.1603	142.7
24	2.5	1	1	0.75	20	4.6835	0	0.1669	143.7
25	5	1	1	0.75	20	3.3468	0.0167	0.1613	144.5
26	10	1	1	0.75	20	2.1414	0.0052	0.1426	145.6
27	15	1	1	0.75	20	1.7002	−0.0005	0.1266	147.0
6	0.5	1	2	0.75	0	5.6541	0	0.1587	291.6
7	0.5	1	2	0.75	0	5.6541	0	0.1587	291.6
8	2.5	1	2	0.75	0	3.6563	0	0.1625	291.5
9	5	1	2	0.75	0	2.3979	0.0132	0.1480	291.5
10	10	1	2	0.75	0	1.3319	0.0043	0.1174	291.6
11	15	1	2	0.75	0	1.0002	0.0009	0.0959	291.7
17	0.5	1	2	0.75	10	5.1309	0	0.1608	311.2
18	2.5	1	2	0.75	10	3.5135	0	0.1855	311.5
19	5	1	2	0.75	10	2.0798	0.0105	0.1759	311.8
20	10	1	2	0.75	10	0.7192	0.0035	0.1438	312.9
21	15	1	2	0.75	10	0.1699	0.0009	0.1191	314.2
28	0.5	1	2	0.75	20	7.6098	0	0.2189	320.8
29	2.5	1	2	0.75	20	4.9665	0	0.2608	321.7
30	5	1	2	0.75	20	3.0255	0.0119	0.2601	322.6
31	10	1	2	0.75	20	0.8629	0.0058	0.2183	325.5
32	15	1	2	0.75	20	0.0624	0.0013	0.1809	328.6
38	0.5	1	3	0.75	0	7.2376	0	0.2401	441.0
39	2.5	1	3	0.75	0	3.8543	0	0.2441	440.8
40	5	1	3	0.75	0	2.0948	0.0203	0.2105	440.5
41	10	1	3	0.75	0	0.8098	0.007	0.1564	439.8
42	15	1	3	0.75	0	0.4853	0.003	0.1278	439.2
43	0.5	1	3	0.75	10	6.9922	0	0.2456	478.1
44	2.5	1	3	0.75	10	3.4328	0	0.2824	478.7
45	5	1	3	0.75	10	1.3606	0.0159	0.2583	479.3
46	10	1	3	0.75	10	−0.4151	0.0071	0.1974	480.2
47	15	1	3	0.75	10	−1.0085	0.0031	0.1584	481.4
48	15	1	3	0.75	10	−1.0085	0.0031	0.1584	481.4
33	0.5	1	3	0.75	20	7.1977	0	0.2933	507.0
34	2.5	1	3	0.75	20	3.8323	0	0.3378	507.8
35	5	1	3	0.75	20	1.2701	0.0154	0.3180	509.0
36	10	1	3	0.75	20	−1.1794	0.0081	0.2522	512.3
37	15	1	3	0.75	20	−2.1879	0.0033	0.2042	516.9
82	0.5	1	4	0.75	10	7.1753	0	0.3040	637.1
83	2.5	1	4	0.75	10	3.1206	0	0.3380	637.2
84	5	1	4	0.75	10	0.6329	0.0255	0.3002	637.1
85	10	1	4	0.75	10	−1.3244	0.0103	0.2307	637.1
86	15	1	4	0.75	10	−1.9323	0.004	0.1838	635.9
67	0.5	0.2	3	0.75	10	6.4853	0	1.2025	474.9
68	2.5	0.2	3	0.75	10	2.9150	0	1.2947	474.8
69	5	0.2	3	0.75	10	1.1045	0.0169	1.2011	474.8
70	10	0.2	3	0.75	10	−0.3408	0.0065	0.9411	475.1
71	15	0.2	3	0.75	10	−0.9525	0.0023	0.7580	475.4
72	0.5	1.5	3	0.75	10	6.8627	0	0.1852	475.0
73	2.5	1.5	3	0.75	10	3.8848	0	0.2106	475.0
74	5	1.5	3	0.75	10	1.4969	0.014	0.1864	475.1
75	10	1.5	3	0.75	10	−0.3709	0.0074	0.1410	476.0
77	0.5	2	3	0.75	10	7.9475	0	0.1430	475.7
78	2.5	2	3	0.75	10	3.9645	0	0.1640	475.6
79	5	2	3	0.75	10	1.4340	0.0193	0.1460	475.7
80	0.5	3	3	0.75	10	7.7987	0	0.0958	475.5
81	2.5	3	3	0.75	10	4.1878	0	0.1102	475.6
49	0.5	1	1	0	10	–	–	–	–
50	2.5	1	1	0	10	–	–	–	–
51	5	1	1	0	10	–	–	–	–
52	10	1	1	0	10	–	–	–	–
53	15	1	1	0	10	–	–	–	–
58	0.5	1	2	0	0	–	–	–	–
59	2.5	1	2	0	0	–	–	–	–
60	5	1	2	0	0	–	–	–	–
61	5	1	2	0	0	–	–	–	–
62	10	1	2	0	0	–	–	–	–
54	0.5	1	2	0	10	–	–	–	–
55	2.5	1	2	0	10	–	–	–	–
56	5	1	2	0	10	–	–	–	–
57	10	1	2	0	10	–	–	–	–
63	0.5	1	2	0	20	–	–	–	–
64	2.5	1	2	0	20	–	–	–	–
65	5	1	2	0	20	–	–	–	–
66	10	1	2	0	20	–	–	–	–

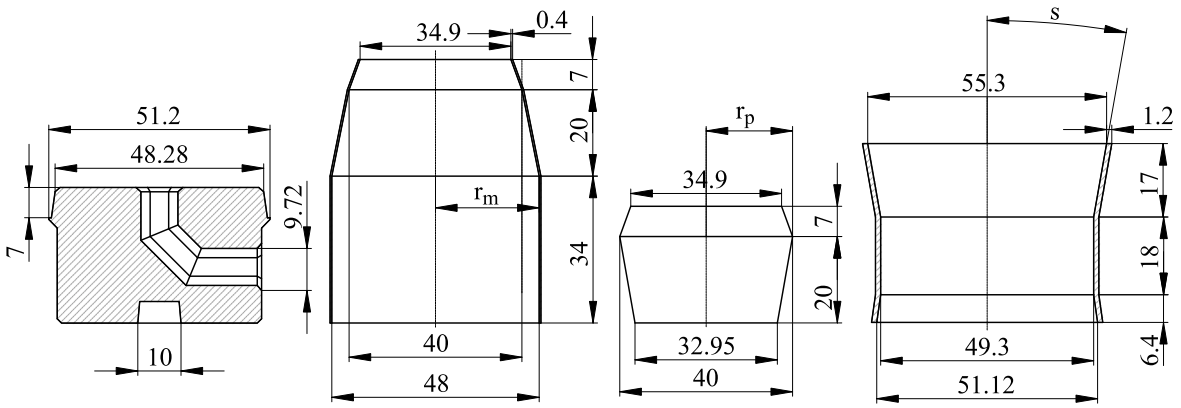

Fig. A.1. Dimensions of rolling-lobe air spring isolator components in mm.

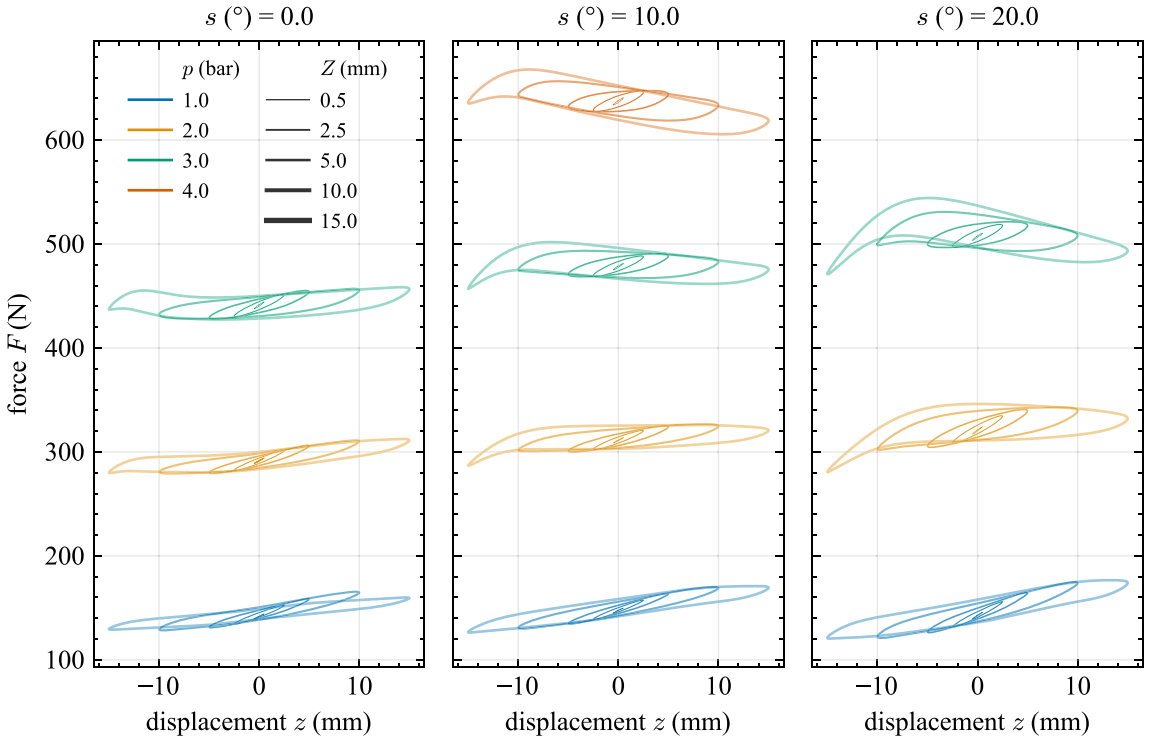

Fig. A.2. Force-displacement curves of all experimentally tested isolator configurations as shown in Table A.1 with $V = 0.75\,\mathrm{dm}^3$ and $f = 1\,\mathrm{Hz}$.

Appendix B. Derivation of optimized piston geometry

To avoid the issue of the membrane bunching up on the piston, the piston geometry is modified to achieve a larger circumference while maintaining the same cross-sectional area. This is accomplished by superimposing a sine wave onto a circle with radius r_p. The resulting parametric equations in terms of parameter u are

$$\begin{aligned} x &= (r_p + a\sin(f_s u))\cos(u) \\ y &= (r_p + a\sin(f_s u))\sin(u) \\ u &\in [0; 2\pi), \end{aligned} \tag{B.1}$$

where f_s is the frequency and a is the amplitude of the sine wave, with x and y representing the coordinates of the curve. The frequency f_s is determined based on the initial diameter of the isolator and remains constant to ensure smooth transitions between cross-sections. A higher f_s improves the distribution of membrane deformation and increases the achievable circumference.

However, a higher frequency also complicates manufacturing due to the smaller feature sizes. In this study, f_s was set to 20 to balance these factors.

The change of the radius r_p plays a crucial role in controlling the air spring's stiffness. To simplify the design, both the membrane and piston radius change angles were set to 10°. This angle choice balances the need for a large rolling radius, which reduces membrane stiffness, against the necessity to limit the increase in membrane circumference. This compromise helps to minimize the extent of modification required for the piston geometry, thereby reducing the risk of membrane bunching. The functions for membrane and piston radius are thus defined as

$$r_m(z) = 20\,\text{mm} + \tan(10°)z \tag{B.2}$$

$$r_p(z) = 20\,\text{mm} - \tan(10°)z\,. \tag{B.3}$$

With the radius function $r_p(z)$ defined, the only free parameter left is the amplitude a. This parameter is optimized across different cross-sections. The objective function for optimization is the difference between the length of the sine curve L and the circumference of the membrane's circular cross-section at each displacement z

$$\text{obj}(a, z) = L(a) - 2\pi r_m(z)\,. \tag{B.4}$$

The length L of the parametric curve is computed by

$$L(a) = \int_0^{2\pi} \sqrt{\left(\frac{\mathrm{d}x}{\mathrm{d}t}\right)^2 + \left(\frac{\mathrm{d}y}{\mathrm{d}t}\right)^2}\,\mathrm{d}u\,. \tag{B.5}$$

The necessary derivatives derived from Eq. (B.1) are

$$\frac{\mathrm{d}x}{\mathrm{d}u} = -a(z)f\,\sin(f_s u)\cos(u) - a(z)\sin(f_s u)\sin(u) + r_p\cos(u) \tag{B.6}$$

$$\frac{\mathrm{d}y}{\mathrm{d}u} = a(z)f\,\sin(f_s u)\sin(u) - a(z)\sin(f_s u)\cos(u) + r_p\sin(u)\,. \tag{B.7}$$

The optimization is performed using a root-finding algorithm, which yields the optimized amplitudes for each cross-section along z. These points are then fitted using a least squares method with a root function of the form

$$a(z) = \lambda_1 \cdot z^{1/\lambda_2} \tag{B.8}$$

where $\lambda_1 \approx 0.3146$ and $\lambda_2 \approx 2.2835$ are determined. The fitted amplitude function is plotted in Fig. 5, where also the shape of the cross sections is shown.

To generate the piston geometry, the function $a(z)$ is substituted into the surface equation derived from Eq. (B.1)

$$\begin{aligned} x &= (r_p - a(z) + a(z)\sin(f_s u))\cos(u) \\ y &= (r_p - a(z) + a(z)\sin(f_s u))\sin(u) \\ z &= v \\ u &\in [0; 2\pi) \\ v &\in [0; 1] \end{aligned} \tag{B.9}$$

where u and v are the surface parameters. This equation defines the surface of the piston, which is then used to create a 3D mesh. The mesh is generated using the Sverchok add-on for Blender and subsequently exported as an STL file.

Appendix C. Supplementary data

Supplementary material related to this article can be found online at https://doi.org/10.1016/j.jsv.2025.119061.

Data availability

The experimental data, the 3D design files as well as the source code to generate the herein presented results are available at https://zenodo.org/doi/10.5281/zenodo.13777799.

References

[1] E.I. Rivin, Passive Vibration Isolation, ASME Press, New York, 2003.
[2] P.M. Alabuzhev, Vibration Protection And Measuring Systems With Quasi-Zero Stiffness, Taylor & Francis, 1989.
[3] G.L. Hermsdorf, S.A. Szilagyi, S. Rösch, E. Schäffer, High performance passive vibration isolation system for optical tables using six-degree-of-freedom viscous damping combined with steel springs, Rev. Sci. Instrum. 90 (1) (2019) 015113, http://dx.doi.org/10.1063/1.5060707.
[4] C.B. Churchill, D.W. Shahan, S.P. Smith, A.C. Keefe, G.P. McKnight, Dynamically variable negative stiffness structures, Sci. Adv. 2 (2) (2016) 1500778, http://dx.doi.org/10.1126/sciadv.1500778.
[5] W.G. Molyneux, Supports for Vibration Isolation, Tech. Rep. 322, Aeronautical Research Council, London, 1957.
[6] H. Li, Y. Li, J. Li, Negative stiffness devices for vibration isolation applications: A review, Adv. Struct. Eng. 23 (8) (2020) 1739–1755, http://dx.doi.org/10.1177/1369433219900311.

[7] W.G. Molyneux, The support of an aircraft for ground resonance tests, Aircr. Eng. Aerosp. Technol. 30 (6) (1958) 160–166, http://dx.doi.org/10.1108/eb032976.
[8] Z. Ma, R. Zhou, Q. Yang, Recent advances in quasi-zero stiffness vibration isolation systems: An overview and future possibilities, Machines 10 (9) (2022) 813, http://dx.doi.org/10.3390/machines10090813.
[9] Y. Xie, F. Niu, J. Sun, L. Meng, Design and analysis of a novel quasi-zero stiffness isolator under variable loads, Math. Probl. Eng. 2022 (2022) e9082752, http://dx.doi.org/10.1155/2022/9082752.
[10] N.Y.P. Vo, T.D. Le, Dynamic analysis of quasi-zero stiffness pneumatic vibration isolator, Appl. Sci. 12 (5) (2022) 2378, http://dx.doi.org/10.3390/app12052378.
[11] Y. Jiang, C. Song, C. Ding, B. Xu, Design of magnetic-air hybrid quasi-zero stiffness vibration isolation system, J. Sound Vib. 477 (2020) 115346, http://dx.doi.org/10.1016/j.jsv.2020.115346.
[12] C.-g. Shuai, B.-y. Li, J.-g. Ma, Z.-h. Yang, A novel low stiffness air spring vibration-isolation mounting system, Shock. Vib. 2022 (1) (2022) 5598689, http://dx.doi.org/10.1155/2022/5598689.
[13] Y. Shi, S. Xu, Z. Li, Y. Wang, Y. Nie, Z. Sun, Dynamic frequency response characteristics of a compound regulative quasi-zero stiffness air spring system, Sci. China Technol. Sci. 66 (7) (2023) 2013–2024, http://dx.doi.org/10.1007/s11431-022-2268-2.
[14] F.P. Bowden, D. Tabor, The Friction and Lubrication of Solids, in: Oxford Classic Texts in the Physical Sciences, Clarendon Press Oxford University Press, Oxford Oxford New York, 2001.
[15] P. Qian, L. Liu, J. Wu, C. Pu, H. Luo, Y. Fu, Q. Zuo, A novel double-acting, air-floating, frictionless pneumatic actuator, Sensors Actuators A: Phys. 362 (2023) 114674, http://dx.doi.org/10.1016/j.sna.2023.114674.
[16] A.I. Oliva, M. Aguilar, V. Sosa, Low- and high-frequency vibration isolation for scanning probe microscopy, Meas. Sci. Technol. 9 (3) (1998) 383–390, http://dx.doi.org/10.1088/0957-0233/9/3/011.
[17] M. Sprengholz, P. Meyer, H. Traub, C. Hühne, Zero stiffness in bellow-type soft pneumatic actuators for modal analysis of flexible aircraft wings, in: ASME 2024 Aerospace Structures, Structural Dynamics, and Materials Conference, American Society of Mechanical Engineers Digital Collection, Renton, WA, USA, 2024, V001T02A011, http://dx.doi.org/10.1115/SSDM2024-121625.
[18] A. Kind, A. Rohde, The harshness of air springs in passenger cars, in: D. Crolla, D.E. Foster, T. Kobayashi, N. Vaughan (Eds.), Encyclopedia of Automotive Engineering, first ed., Wiley, 2014, pp. 1–17, http://dx.doi.org/10.1002/9781118354179.auto015.
[19] G. Sidebotham, An Inductive Approach to Engineering Thermodynamics, in: Mechanical Engineering Series, Springer International Publishing, 2022.
[20] Y. Hu, J. Zhang, J. Long, Influence of rubber's viscoelasticity and damping on vertical dynamic stiffness of air spring, Sci. Rep. 13 (1) (2023) 9886, http://dx.doi.org/10.1038/s41598-023-36904-9.
[21] M. Wu, Z. Chen, D. Liu, J. Wang, H. Yin, K. Dou, D. Li, Y. Zhang, C. Zhang, Y. Wei, A theoretical model of amplitude-dependent dynamical stiffness for cord-rubber air springs, Proc. Inst. Mech. Eng. L: J. Mater.: Des. Appl. 237 (2) (2023) 425–436, http://dx.doi.org/10.1177/14644207221117270.
[22] L. Xiao, X. Sun, L. Cheng, X. Yu, A 3D-printed Quasi-Zero-Stiffness isolator for low-frequency vibration isolation: Modelling and experiments, J. Sound Vib. 577 (2024) 118308, http://dx.doi.org/10.1016/j.jsv.2024.118308.
[23] A. Carrella, M. Brennan, T. Waters, V. Lopes, Force and displacement transmissibility of a nonlinear isolator with High-Static-Low-Dynamic-Stiffness, Int. J. Mech. Sci. 55 (1) (2012) 22–29, http://dx.doi.org/10.1016/j.ijmecsci.2011.11.012.
[24] C.M. Harris, A.G. Piersol (Eds.), Harris' Shock and Vibration Handbook, fifth ed., in: McGraw-Hill Handbooks, McGraw-Hill, New York, 2002.
[25] M.-Q. Niu, L.-Q. Chen, Analysis on nonlinear stiffness isolators revealing damping thresholds, Commun. Nonlinear Sci. Numer. Simul. 128 (2024) 107536, http://dx.doi.org/10.1016/j.cnsns.2023.107536.
[26] J.-H. Lee, K.-J. Kim, A method of transmissibility design for Dual-Chamber pneumatic vibration isolator, J. Sound Vib. 323 (1) (2009) 67–92, http://dx.doi.org/10.1016/j.jsv.2008.12.028.
[27] M. Heertjes, N. van de Wouw, Nonlinear dynamics and control of a pneumatic vibration isolator, J. Vib. Acoust. 128 (4) (2005) 439–448, http://dx.doi.org/10.1115/1.2128642.
[28] N.Y.P. Vo, M.K. Nguyen, T.D. Le, Analytical study of a pneumatic vibration isolation platform featuring adjustable stiffness, Commun. Nonlinear Sci. Numer. Simul. 98 (2021) 105775, http://dx.doi.org/10.1016/j.cnsns.2021.105775.
[29] J. Kim, Y. Jeon, S. Um, U. Park, K.-S. Kim, S. Kim, A Novel Passive Quasi-Zero Stiffness Isolator for ultra-precision measurement systems, Int. J. Precis. Eng. Manuf. 20 (9) (2019) 1573–1580, http://dx.doi.org/10.1007/s12541-019-00149-2.
[30] H.J. Qi, M.C. Boyce, Stress–strain behavior of thermoplastic polyurethanes, Mech. Mater. 37 (8) (2005) 817–839, http://dx.doi.org/10.1016/j.mechmat.2004.08.001.
[31] D.R. Moss, Pressure Vessel Design Manual: Illustrated Procedures for Solving Major Pressure Vessel Design Problems, third ed., Gulf Professional Pub, Amsterdam Boston, 2004.
[32] K. Wang, J. Zhou, Y. Chang, H. Ouyang, D. Xu, Y. Yang, A nonlinear ultra-low-frequency vibration isolator with dual Quasi-Zero-Stiffness Mechanism, Nonlinear Dynam. 101 (2) (2020) 755–773, http://dx.doi.org/10.1007/s11071-020-05806-0.